# Tau induces blood vessel abnormalities and angiogenesis-related gene expression in P301L transgenic mice and human Alzheimer's disease

Rachel E. Bennett[a], Ashley B. Robbins[a], Miwei Hu[a], Xinrui Cao[b], Rebecca A. Betensky[b], Tim Clark[a], Sudeshna Das[a], and Bradley T. Hyman[a,1]

[a]Department of Neurology, MassGeneral Institute for Neurodegenerative Disease, Massachusetts General Hospital, Harvard Medical School, Charlestown, MA 02129; and [b]Department of Biostatistics, Harvard T.H. Chan School of Public Health, Boston, MA 02115

Edited by Napoleone Ferrara, University of California, San Diego, La Jolla, CA, and approved December 20, 2017 (received for review June 9, 2017)

**Mixed pathology, with both Alzheimer's disease and vascular abnormalities, is the most common cause of clinical dementia in the elderly. While usually thought to be concurrent diseases, the fact that changes in cerebral blood flow are a prominent early and persistent alteration in Alzheimer's disease raises the possibility that vascular alterations and Alzheimer pathology are more directly linked. Here, we report that aged tau-overexpressing mice develop changes to blood vessels including abnormal, spiraling morphologies; reduced blood vessel diameters; and increased overall blood vessel density in cortex. Blood flow in these vessels was altered, with periods of obstructed flow rarely observed in normal capillaries. These changes were accompanied by cortical atrophy as well as increased expression of angiogenesis-related genes such as *Vegfa*, *Serpine1*, and *Plau* in CD31-positive endothelial cells. Interestingly, mice overexpressing nonmutant forms of tau in the absence of frank neurodegeneration also demonstrated similar changes. Furthermore, many of the genes we observe in mice are also altered in human RNA datasets from Alzheimer patients, particularly in brain regions classically associated with tau pathology such as the temporal lobe and limbic system regions. Together these data indicate that tau pathological changes in neurons can impact brain endothelial cell biology, altering the integrity of the brain's microvasculature.**

Alzheimer's disease | blood vessels | brain microvessels | tau | angiogenesis

Alzheimer's disease (AD) pathology is characterized by amyloid beta plaques, tau-containing neurofibrillary tangles, and neuronal cell death. Mounting evidence indicates that, as assessed in life by MRI scans or at autopsy by neuropathological evaluation, "pure" AD is substantially less common than mixed dementias, in which tangles and plaques are accompanied by vascular changes (1, 2). Common conditions including atherosclerosis, hypertension, hypercholesterolemia, and diabetes contribute to cerebral vasculature alterations and worsen disease (3–6). These changes have been interpreted as incidental co-occurrence of common age-related illnesses, in which separate diseases contribute to neural system dysfunction or neuronal loss. An alternative possibility is that AD pathology directly promotes vascular structural or functional changes. For example, measures of cerebral perfusion in disease indicate that diminished blood flow correlates with the development of tau pathology (7, 8), and amyloid deposition near vessels (cerebral amyloid angiopathy, CAA) is associated with MRI signatures of small vessel disease (9).

To directly test the hypothesis that neurofibrillary lesions can impact vascular biology, we examined cortical vessels over time in the Tg4510 tauopathy model. These animals develop progressive cortical tangles and ultimately neuronal loss and atrophy with aging, approximating the kind of neuronal damage observed in AD (10). We performed in vivo imaging to assess blood vessel changes in these tau-overexpressing mice and found marked morphological changes including apparent neovascularization that occurred in concert with neuronal loss. Further studies demonstrated up-regulation of vascular remodeling genes detected in isolated endothelial cells and indicate a noncell autonomous effect of tau expression in neurons affecting endothelial cell neurovascular biology. Hypotheses based on these results were evaluated in large databases of gene expression in AD brain, with results strongly supporting the idea that these changes are present in human cortex as well. We suggest that tau-associated lesions contribute pathophysiologically to some of the vascular abnormalities commonly observed in AD brain.

## Methods

**Animals.** All animals were handled and housed according the protocols of Massachusetts General Hospital and the McLaughlin Research Institute. Strains used for these experiments included FVB-Tg4510xB6.TgCK-tTA (Tg4510 mice) and (APP/PSEN)85 × rTg4510 (FVBB6F1rTg4510(App/PSEN1)85) (APP/PS1-Tg4510 mice). Tg21221 mice were also used from the (APP/PSEN)85xrTg21221(FVBB6F1rTg21221(App/PSEN1)85) mouse line. Further details regarding these mouse lines have been previously published (10–12).

**Human Tissue Selection.** Blocks of frozen frontal cortex were obtained from the Neuropathology Core of the Massachusetts Alzheimer's Disease Research Center (ADRC) at the MassGeneral Institute for Neurodegenerative Disease. Cases were assessed by a neuropathologist and were matched for age and gender. "Control" cases ($n = 3$) were selected that had received Braak staging scores of O/I/II, had sparse plaque pathology, and were rated as having low probability of AD by National Institute on Aging and the Alzheimer's Association (NIA-AA) criteria. AD cases ($n = 3$) were selected that had received Braak staging scores of V/VI, had frequent plaques and were rated as having intermediate or high probability of AD.

**In Vivo Imaging.** When mice reached the appropriate age for these studies (2, 9, 12, 15, or 18 mo), they were anesthetized by i.p. injection of 100 mg/kg ketamine and 10 mg/kg xylazine. Lidocaine was injected into the scalp, and then an incision was made over the midline. A craniotomy was performed over the somatosensory cortex of ∼4 mm in diameter. The craniotomy was filled with PBS, and a sterile 8-mm glass coverslip was glued to the skull with dental cement. Mice received i.v. injections of 200 μL of fluorescein-conjugated dextran (70,000 MW) at a concentration of 12.5 mg/mL (Invitrogen) or, to perform labeling of circulating leukocytes, 100 μL fluorescein–dextran and 100 μL 0.05% rhodamine 6G (Sigma-Aldrich) in PBS (13).

### Significance

This work provides evidence that the protein tau induces changes in blood vessels distinct from the effects of amyloid beta on vasculature and indicates a previously unknown pathway by which pathological tau may accelerate cognitive decline in Alzheimer's disease.

Author contributions: R.E.B. and B.T.H. designed research; R.E.B., A.B.R., and M.H. performed research; T.C. contributed new reagents/analytic tools; R.E.B., A.B.R., M.H., X.C., R.A.B., T.C., S.D., and B.T.H. analyzed data; and R.E.B. and B.T.H. wrote the paper.

The authors declare no conflict of interest.

This article is a PNAS Direct Submission.



[1]To whom correspondence should be addressed. Email: bhyman@mgh.harvard.edu.

This article contains supporting information online at www.pnas.org/lookup/suppl/doi:10.1073/pnas.1710329115/-/DCSupplemental.

Two-photon imaging was performed using an Olympus imaging system (Fluoview1000) equipped with water immersion lens (25×, N.A. = 1.05) and a Ti:sapphire laser (MaiTai, Spectra Physics). Fluorescence was excited at 800 nm, and emitted light was detected through 520–560-nm and 575–630-nm filters (Hamamatsu). For quantification of blood vessels, six regions of the motor/somatosensory cortex were imaged at 3× zoom (169 μm × 169 μm). Fields were randomly selected, avoiding large arterioles or veins that took up more than 1/3 the field of view so as to avoid overestimating the size of the capillary bed. Each *z* stack began 50 μm below the cortical surface and contained 50 planes acquired in 2-μm steps (100 μm total depth). Each group of mice was imaged either on the same day or on consecutive days using the same imaging settings. For time-lapse imaging, scan speed was increased to 2 μs per pixel with 3× or 6× zoom, and frames were captured for 20–30 s.

Mice were acutely imaged within the hour and were then killed by isofluorane and cardiac perfusion. The cortex was dissected from the left hemisphere and frozen for protein or RNA extraction, and the right hemisphere was fixed in 4% paraformaldehyde and reserved for immunohistochemistry.

**Western Blotting.** The cortex from mouse or human brain was Dounce-homogenized in 200 μL PBS with protease inhibitors and spun at 3,000 × *g* for 10 min at 4 °C. The supernatant containing soluble proteins was reserved for Western blotting. To prepare samples for Western blot, 10 μg protein was mixed with lithium dodecyl sulfate sample buffer and reducing agent (Invitrogen) and was heated at 95 °C for 5 min. Samples were loaded on a 1.0-mm 4–12% Bis–Tris gel that was run at 120 V for 1.5 h in Mes buffer (Invitrogen). Proteins were then transferred to nitrocellulose membranes (Bio-Rad) at 90 V for 1.5 h. The resulting membrane was blocked in Odyssey blocking buffer (LiCor) and probed with antibodies overnight. Primary antibodies used in this study included rabbit anti-plasminogen activation inhibitor (PAI-1) (cat. no. ab28207 RRID:AB_777021; Abcam), rabbit anti–PAI-1 (recognizes human, cat. no. ab20562 RRID:AB_470312; Abcam), chicken anti-Actin (cat. no. SAB3500350 RRID:AB_10638013; Sigma-Aldrich), and mouse anti-NeuN (cat. no. MAB337 RRID:AB_2313673; Millipore). After washing with Tris-buffered saline (TBS) with Tween 20, infrared-conjugated secondary antibodies were incubated in blocking buffer for 1.5 h and were then imaged using a LiCor Imaging Station.

For quantification of Western blots, a rectangular selection was made around bands of interest in ImageJ. Using the gel analyzer tools, lanes were plotted and the area of each band peak was measured. Values for each protein were normalized to the actin loading control from the same blot.

**Histology.** To assess cortical thickness, fixed hemispheres were equilibrated in 30% sucrose overnight and then were sliced into 40 μm-thick coronal sections on a freezing microtome. Eight sets of sections were collected so that each contained sections sampled at 320-μm intervals. Sections were rinsed in TBS three times, then mounted on microscope slides and allowed to air-dry. Once dry, slides were immersed in cresyl violet (FD Neurotech) for 5 min, then rinsed in tap water, and dehydrated through ascending ethanol solutions and xylene. Slides were cover-slipped with Cytoseal XL (Millipore) and imaged using a bright-field microscope. To measure cortical thickness, images were captured of cortex starting at the head of the hippocampus and including the next four posterior sections. This region corresponded to the area imaged by two-photon microscopy. Cortex was measured by drawing a line perpendicular to the edge of the tissue to the dorsal surface of the external capsule. Three measures were made per section for a total of 12 measurements per animal to yield the average cortical thickness.

For immunofluorescence, free-floating sections were first rinsed briefly in TBS and then blocked in 3% normal goat serum (Vector Laboratories) in TBS containing 0.25% Triton-X (Sigma-Aldrich) for 30 min. Sections were incubated overnight in primary rabbit anti-PAI-1 and mouse monoclonal MC1 anti-tau (Peter Davies, Albert Einstein College of Medicine, New York; cat. no. MC1 RRID:AB_2314773). The following day, sections were rinsed in TBS and incubated in goat anti-rabbit Cy3 and goat anti-mouse Alexa 488 for 3 h and then rinsed and incubated overnight in rabbit anti–Iba-1 (cat. no. 016–20001 RRID:AB_839506; Wako). Goat anti-rabbit Alexa 647 was applied the following day, and then sections were rinsed and mounted on microscope slides, coverslipped with Fluormount G, and imaged. For blood vessel labeling, Dylight 649-conjugated Lycopersicon Esculentum (Tomato) Lectin (cat. no. DL11-78 RRID:AB_2336416; Vector Laboratories) was applied overnight.

**Blood Vessel Data Analysis.** For measurement of the number of blood vessels and diameters, a blinded investigator (M.H.) counted the number of unique blood vessel branches in each *z* stack using ImageJ (NIH v.1.49m) and drew a line perpendicular to the long axis of the blood vessel to measure its diameter at its widest point. Multiple planes per *z* stack were compared to avoid counting the same blood vessel more than once. For automated measurement of blood vessel density, a custom macro was created in ImageJ that uses the 3D Objects Counter and Skeletonize (2D/3D) plugins. Gaussian smoothing and a default threshold value of 24 was applied to all images. Using these tools, we obtained measures of the total volume of blood vessels per total imaging volume (cubic microns) as well as total length of blood vessels per imaged volume (microns per cubic microns). To normalize these values to account for cortical atrophy, the average cortical thickness for each control mouse group was first calculated. This value was set to 1 and was divided by the value of each individual mouse. Blood vessel density and length measures were then multiplied by this cortical atrophy measure (e.g., no loss would result in multiplication by 1 and no change in value, while smaller cortices would be multiplied by smaller values).

To estimate the percentage of blocked blood vessels, 6× *z* stacks of capillaries were examined from mice, and a vessel was considered "blocked" if red blood cells or rhodamine 6G-labeled cells were observed in the same location in at least two consecutive sections (an indicator that no movement had occurred; frames were captured at 0.5-s intervals). The total number of unique blood vessel branches were counted per field as described above to yield the overall percentage of blocked blood vessels per mouse.

The datasets described above were first tested for normality using Shapiro–Wilk normality tests, determining our use of Student's *t* tests versus Mann–Whitney *U* tests. The test used is indicated in the results, and *P* values less than 0.05 are reported as significant. One-way ANOVA was used to assess significance in the APP/PS1-Tg4510 line with post hoc Sidak's multiple comparisons tests.

**Brain Dissociation.** For separation of specific cell types from the mouse brain, mice were deeply anesthetized by isofluorane and killed by rapid decapitation. Brains were removed and cut with a razor blade into six to eight slices excluding the cerebellum and brainstem. Tissue slices were dissociated into cell suspensions using an Adult Brain Dissociation kit (mouse and rat; Miltenyi Biotec) according to the manufacturer's instructions and a gentleMACS dissociator. Following dissociation, cell suspensions were incubated with either CD11b (microglia) or with ASCA-2 (astrocytes) and then CD31 (endothelial cells) beads (Miltenyi Biotec). Isolated cells were immediately pelleted by centrifugation, and RNA isolation was performed.

**RNA Isolation and qPCR.** RNA was isolated using an RNeasy Mini kit (Qiagen) according to the manufacturer's instructions. RNA pellets were resuspended in 30 μL of DNase, and RNase free water in the final step. RNA yield was quantified using a NanoDrop spectrophotometer (ThermoFisher). A reverse transcription kit ($RT^2$ First Strand Kit; Qiagen) was used for cDNA synthesis. The cDNA synthesis reaction was combined with an $RT^2$ SYBR Green qPCR Mastermix (Qiagen) for loading onto a qPCR plate. All qPCR results were obtained using a Mouse Hypoxia Signaling Pathway $RT^2$ Profiler PCR Array (96-well format; Qiagen). Genes assessed in this array are listed in Table S1. A qPCR components mix, containing $RT^2$ First Strand Synthesis reaction and $RT^2$ SYBR Green Mastermix, was loaded into the array plates using a multichannel pipette. Provided optical thin-walled caps were used to seal the PCR plate, and the contents were briefly spun to ensure all contents were at the bottom of the wells. The qPCR reactions were performed in a Bio-Rad CFX96 real-time cycler [10 min at 95 °C, 40 cycles (15 s at 95 °C; 1 min at 60 °C)].

The results of each $RT^2$ Profiler PCR Plate were quality checked by analyzing $C_T$ values for genomic DNA contamination, as well as a reverse transcription control (RTC) and positive PCR control (PPC) following the manufacturer's instructions. Each $RT^2$ Profiler PCR Array contains five housekeeping genes (*Actb*, *B2m*, *Gapdh*, *Gusb*, and *Hsp90ab1*). The geometric mean of the $C_T$ values for the five housekeeping genes was calculated and subtracted from the $C_T$ value of each gene of interest to obtain $\Delta C_T$ values. The $\Delta C_T$ values were averaged across triplicates of each condition. $\Delta\Delta C_T$ values were calculated by subtracting the average $\Delta C_T$ of the control samples from the average $\Delta C_T$ of the experimental samples. Fold change (or relative quantitation, RQ, value), from control to experimental conditions, was calculated as $2^{(-\Delta\Delta CT)}$. Volcano plots were derived by using the negative log base 10 of the *P* value and the log base 2 of the RQ values (fold change).

For validation of CD31, CD11b, and ASCA-2 cell types isolated with microbeads, a qPCR validation plate was prepared using Quantitect Primer Assays for *Actb*, *Gapdh*, *Hprt*, *MapT*, *Grin*, *Camk2a*, *Pecam1*, *Cx3cr1*, *Aq4*, and *Gfap* (Qiagen). cDNA synthesis from RNA samples was performed using a Quantitect Reverse Transcription kit (Qiagen) and 20 ng of RNA per sample. The cDNA synthesis reactions were then added to Quantitect SYBR green mastermix (Qiagen) in a 96-well qPCR plate, sealed with optically clear flat seal caps (ThermoFisher), and spun at 300 × *g* briefly. All qPCR reactions were performed in a Bio-Rad CFX96 real-time cycler, according to manufacturer's instructions. The geometric mean of the $C_T$ values for the three housekeeping genes—*Actb*, *Gapdh*, and *Hprt*—were taken and used to calculate the $\Delta C_T$ for

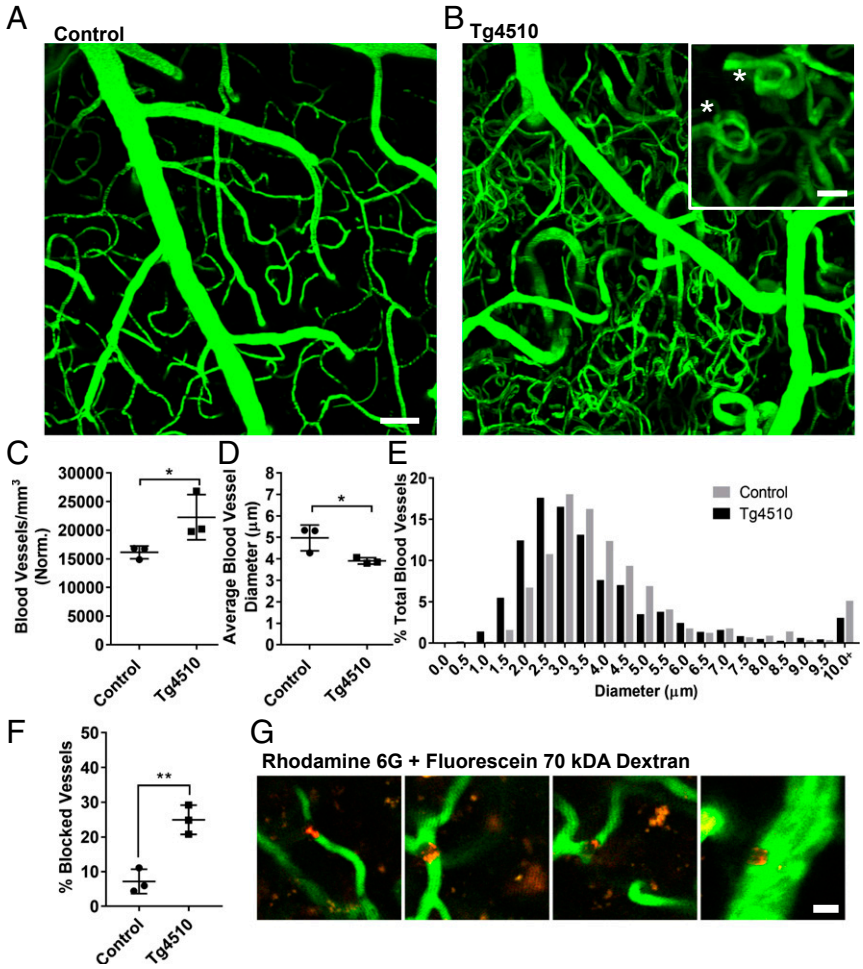


**Fig. 1.** Altered blood vessel morphology, number, and density in aged Tg4510 mice. In vivo two-photon microscopy of 15-mo-old wild-type control (*A*) and Tg4510 (*B*) mice injected with i.v. fluorescein–dextran revealed abnormal spiral morphologies in Tg4510 mice (*B*, *Inset*, asterisks denote spirals). [Scale bar, (*A* and *B*) 50 μm and (*B*, *Inset*) 20 μm.] Images were captured from multiple fields of view per animal, and the average number of blood vessels per cubic millimeters was calculated (*C*) in addition to the average diameter of vessels per mouse (*D*). (*E*) A histogram of average diameter measures in each genotype shows a shift toward smaller-diameter vessels in Tg4510 mice. Individual diameter measures per mouse can be found in Fig. S1. (*F*) The percentage of blood vessels without red blood cell flow is indicated. (*G*) Representative images of small-diameter vessels with rhodamine-6G–labeled adherent leukocytes appearing red against green fluorescein–dextran-labeled sera. (Scale bar, 10 μm.) $n = 3$ mice per genotype. $^*P < 0.05$, $^{**}P < 0.01$.

each gene of interest. A total cortex RNA sample was used as a comparison for cell-type enrichment. The $\Delta\Delta C_T$ values were calculated by subtracting the $\Delta C_T$ value of the total cortex RNA sample from the $\Delta C_T$ of the cell-type enriched sample. Fold change was calculated as described above. A complete set of qPCR data including all genes and analyses can be found in Dataset S1.

Data from qPCR arrays were confirmed to be approximately normally distributed through inspection of histograms of the ΔCT values for Tg4510 and wild-type control mice. Variances were calculated for each genotype, and then pooled variances for each gene across the wild-type control and Tg4510 groups were determined for each separate dataset (Total RNA, Asca-2, CD11b, CD31 cells). *P* values were computed via two-sample *t* tests between Tg4510 and wild-type controls for each of the 84 genes. In the case of Asca-2 cells, no *P* values were significant at $P < 0.05$ for any gene. In the other three datasets, the *q* values, the minimum false discovery rate (FDR) at which a test is significant, were determined (qvalue package in R version 2.4.2, https://github.com/StoreyLab/qvalue). These *q* values were considered significant using a threshold of 0.05. *P* values, *q* values, and local FDRs are reported in Dataset S1.

**Human RNA Data Analysis.** RNA expression data were obtained from the Accelerating Medicines Partnership Alzheimer's Disease (AMP-AD) knowledge portal (https://www.synapse.org/#!Synapse:syn2580853/wiki/409841). Processed RNA-sequencing (RNA-seq) and microarray data were downloaded from the Mount Sinai Brain Bank (MSBB) AD Cohort and the Religious Orders Study and Memory and Aging Project (ROS/MAP) Study. In total, there are 19 different brain regions in the set; 5 of these regions have both RNA-seq and microarray data. The details of the 25 datasets are presented in Dataset S2. The samples were grouped by the Braak score, which assesses the distribution of tau neurofibrillary tangles in the subject's brain (14). Differential expression between subjects in B3 stages (Braak V/VI) and B1 stages (Braak 0/I/II) was analyzed using the Limma package in R (15). The expression of 14 genes (*Egr1*, *Pgf*, *Met*, *Hmox1*, *Plau*, *Lax*, *Lgals3*, *Mmp9*, *Vegfa*, *Slc16a3*, *Eif4ebp1*, *Atr*, *Serpine1*, and *Hif1an*) was examined. If a gene had multiple probes within a dataset, we selected the probe with the highest absolute value of differential expression. Each dataset included values for all 14 genes except in two instances where *Hif1AN* and *Lax* were unavailable. For each gene, in the first stage of analysis, for each of the five brain regions for which there were multiple datasets (RNA-seq and microarray or multiple cohorts), we adjusted the *P* values for the multiple analyses using the Benjamini and Hochberg method (16). In the second stage, we again adjusted the *P* values across the 25 datasets that represent the 19 brain regions (note that 5 of these were preadjusted in the first stage). For the purpose of selection for visual display, we used a FDR threshold of 0.25. All results for the differential expression analysis are listed in Dataset S2.

## Results

**Increased Number of Small-Diameter Blood Vessels in Aged Tau Mice.** First, we performed in vivo measurements of blood vessels from Tg4510 mice, which overexpress tau with the P301L familial frontotemporal dementia mutation. These mice exhibit striking

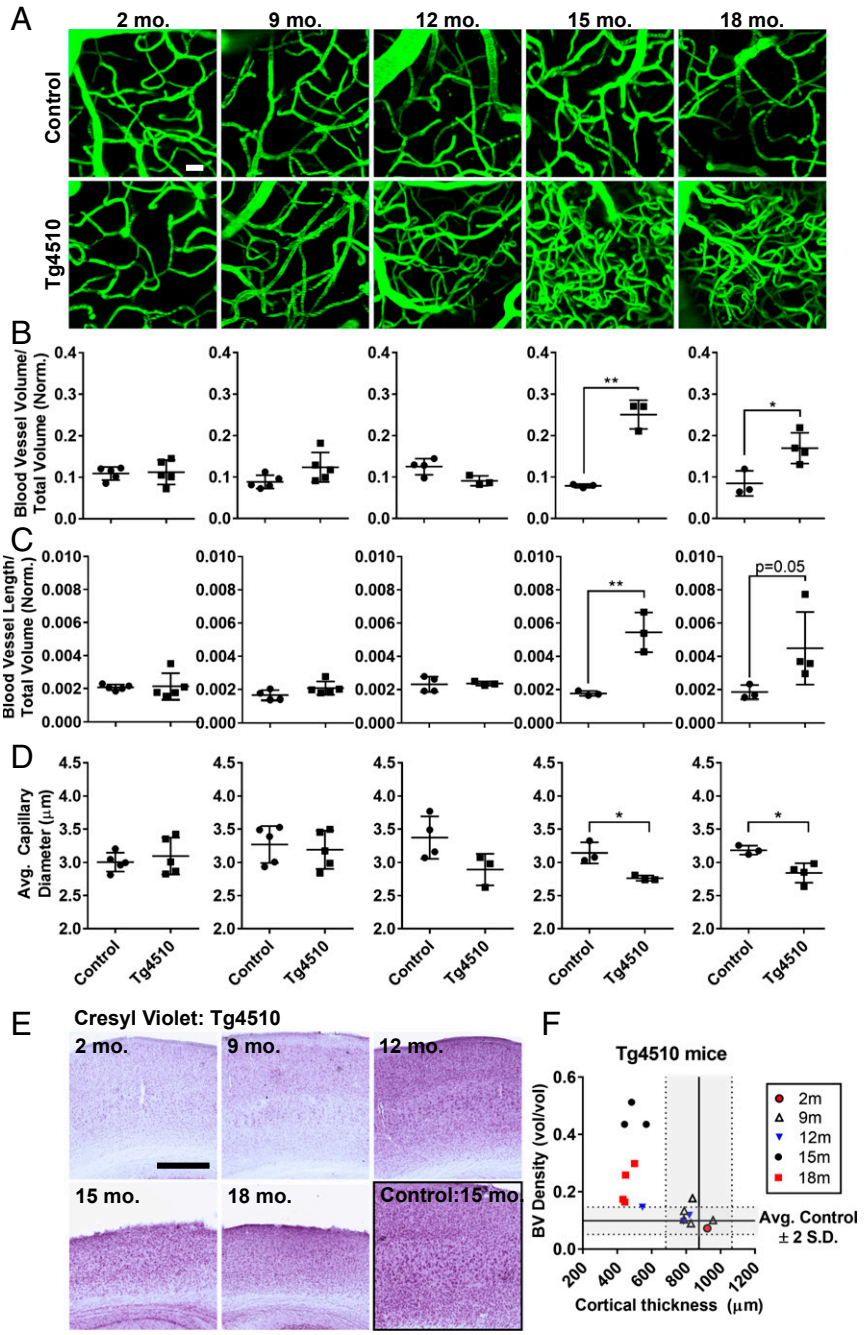


**Fig. 2.** Time course of cortical blood vessel changes. (*A*) Separate groups of wild-type control and Tg4510 mice were imaged at 2, 9, 12, 15, or 18 mo of age ($n$ = 3–5 mice per group). (Scale bar, 20 μm.) Blood vessel (*B*) density, (*C*) length, and (*D*) capillary diameters were compared at each age. (*E*) Cresyl violet-stained sections were used to measure cortical atrophy. (Scale bar, 400 μm.) (*F*) Nonnormalized blood vessel density plotted against cortical thickness highlights the relationship between these variables in Tg4510. The blood vessel density and cortical thickness ±2 SDs in control animals are indicated by shaded regions for a reference. *$P < 0.05$, **$P < 0.01$.

tau tangle pathology that is progressive in the cortex and hippocampus initially detectable at 4 mo and subsequent gliosis and neuronal loss (10). In the initial study, we injected i.v. fluorescein-conjugated 70 kDa of dextran and imaged the vasculature from aged, 15-mo-old Tg4510 mice using two-photon microscopy (Fig. 1 *A–E*). Images from control mice (Fig. 1*A*) were markedly different from those obtained from Tg4510 mice (Fig. 1*B*), where an increased number of blood vessels were observed including many that appeared to have tight turns and spiral paths (Fig. 1*B*). Images from these mice were counted manually by a blinded and impartial observer who quantified the number of unique branches from each image (Fig. 1*C*) and the widest point of each branch (Fig. 1*D*) in each $z$ stack. To account for cortical atrophy, which could be one explanation for the increased apparent density of blood vessels, we measured cortical thickness ex vivo from multiple sections per animal and normalized measurements to the value for the vasculature for each mouse. This confirmed our observation that there were more blood vessels per cubic millimeter of cortex even when taking into account the reduced size of the cortex (Fig. 1*C*, Student's $t$ test $P = 0.03$, 95% confidence

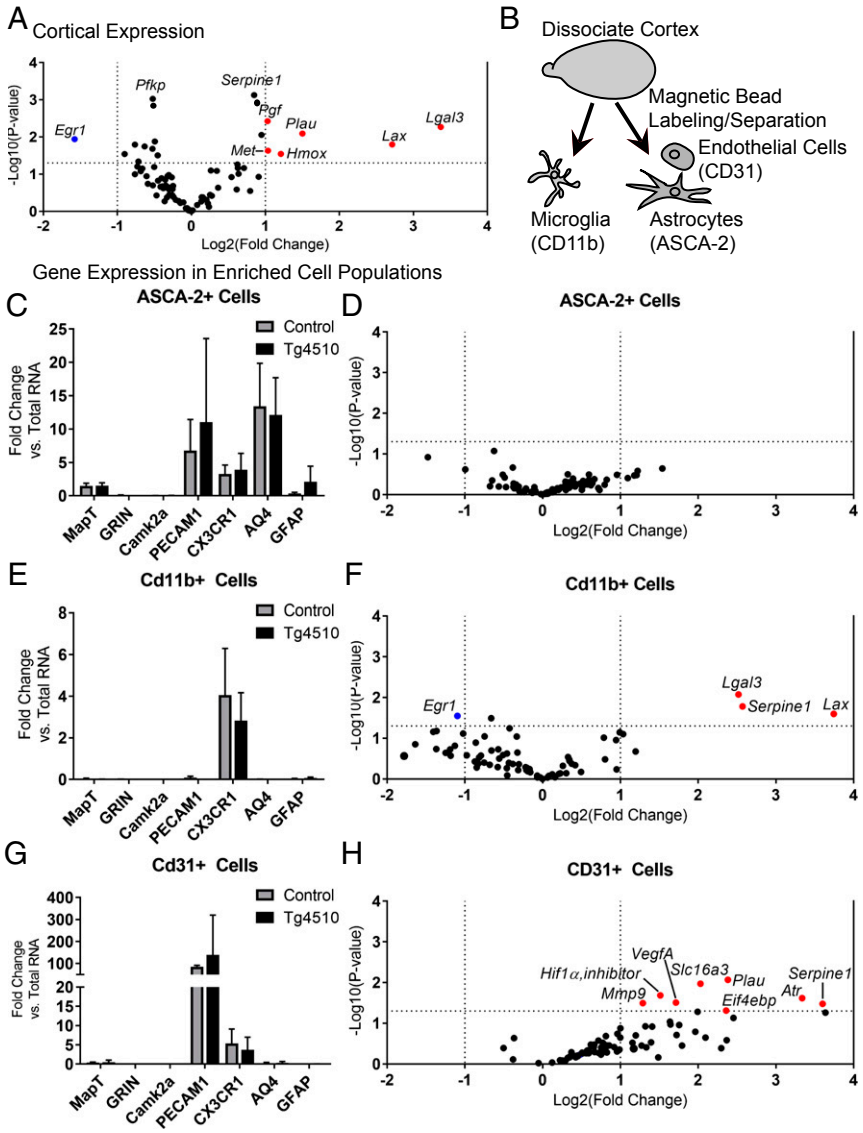


**Fig. 3.** Altered hypoxia and angiogenesis genes in Tg4510 mice. Quantitative PCR arrays examining 84 genes related to hypoxia and angiogenesis were assessed using samples from $n = 3$ Tg4510 and $n = 3$ wild-type control mice. The results of total cortex expression changes in Tg4510 mice are plotted (*A*), where significant *P* values appear above the dotted line and fold changes >2 appear to the left or right of the dotted line. (*B*) In two separate cohorts of mice, whole hemispheres were dissociated into a cell suspension that was further separated into either microglial cells or astrocytes and then endothelial cells. The purity of each cell population was assessed by cell type-specific qPCR (*C*, *E*, and *G*) before running on the hypoxia and angiogenesis gene array (*D*, *F*, and *H*).

interval, CI: [−435 to 12,707]). Additionally, average blood vessel diameter was reduced from 4.97 ± 0.35 μm in controls to 3.90 ± 0.08 μm in Tg4510 mice (Fig. 1*D*, Student's *t* test $P = 0.04$, 95% CI: [−2.06 to −0.08], and Fig. 1*E*).

Surprisingly, many of these small-diameter blood vessels—including those with spiral-type paths—appeared to be functional, and the passage of red blood cells was observed (Movie S1). Other blood vessels appeared to contain only plasma. Further investigation of these plasma-only–containing vessels indicated that blockage by adherent leukocytes may be partially to blame as rhodamine 6G-labeled cells were frequently found upstream (Movie S2). Blocked vessels occasionally resumed flow during a 30-s observation period (Movie S3). This apparent dysfunction was not exclusive to Tg4510 mice and was occasionally seen in littermate controls. It was, however, only observed in small, <4 μm in diameter, blood vessels. Blocked blood vessels, in which stationary cells were identified in at least two consecutive frames during imaging, were observed in 25 ± 4% of capillaries in Tg4510 mice compared with 7 ± 3.5% in control mice (Fig. 1 *F* and *G*, Student's *t* test $P = 0.005$, 95% CI: [9.02–26.5]).

**Time Course of Blood Vessel Density Changes.** To better understand when these changes occur in relation to neuronal loss, we examined separate groups of 2-, 9-, 12-, 15-, and 18-mo-old Tg4510 mice (Fig. 2). Blood vessels were imaged as before, and a custom ImageJ script was used to quantify total blood vessel volume per total imaged volume (Fig. 2*B*) and blood vessel length per volume normalized to cortical thickness (Fig. 2*C*). Blood vessel volume was unchanged at 2, 9, and 12 mo but was increased at 15 (Student's *t* test, $P = 0.001$, 95% CI: [0.12–0.23]) and 18 ($P = 0.023$, 95% CI: [0.02–0.15]) mo of age. Length was also increased at 15 (Student's *t* test, $P = 0.006$, 95% CI: [0.002–0.006]) and 18 (Mann–Whitney *U* test, $P = 0.03$, 95% CI: [0.0006–0.006]) mo of age but

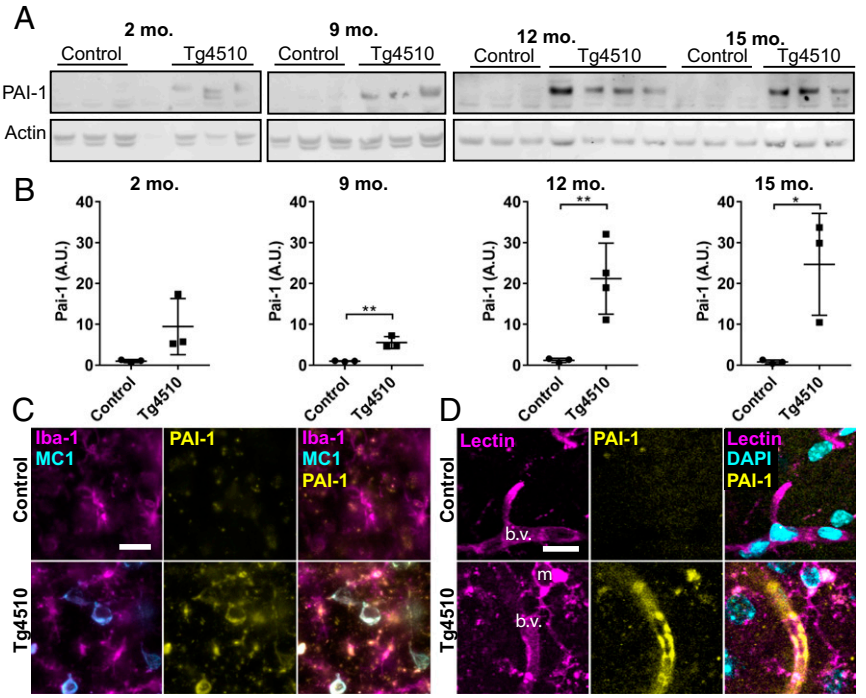


**Fig. 4.** PAI-1 expression in tau-overexpressing mice. (*A*) PAI-1, the protein product of *Serpine1*, was detected in 2-, 9-, 12-, and 15-mo cortical homogenates of Tg4510 mice by Western blotting ($n$ = 3–4 mice per genotype). The 2- and 9-mo samples were run on one blot and 12- and 15-mo samples on a second. (*B*) PAI-1 bands were quantified by densitometry and normalized to actin loading control. (*C*) Coronal sections from 15-mo-old mice were probed for microglia (Iba-1), tau (MC1), and PAI-1. In Tg4510 mice, colocalization of PAI-1 was most prominent in microglial cells and cells containing misfolded MC1-positive tau aggregates. (Scale bar, 20 μm.) (*D*) Additional labeling for both microglia (m) and blood vessels (b.v.) using tomato-lectin indicates PAI-1 is also localized to blood vessels in 15-mo Tg4510 mice. DAPI was used to label nuclei. (Scale bar, 10 μm.) Error bars represent ±SDs. $^*P < 0.05$, $^{**}P < 0.01$. A.U., arbitrary unit.

not in younger mice. Density and blood vessel length remained stable across ages in control mice.

We also measured blood vessel diameters in these mice, focusing on small microvessels <10 μm in diameter. This size cutoff corresponds with existing literature defining capillaries in the intact rodent brain (17). In agreement with our initial cohort, diameters (Fig. 2*D*) were significantly decreased in 15-mo-old mice (Student's $t$ test, $P = 0.015$, 95% CI: [−0.59 to −0.22]) and continued to be reduced at 18 mo of age ($P = 0.013$, 95% CI: [−0.62 to −0.14]). No change in diameter in Tg4510 mice compared with control mice was detected at younger ages.

Cortical thickness measurements were made using cresyl violet-stained sections (Fig. 2*E*). Plotting cortical thickness versus blood vessel density in Tg4510 mice, it is apparent that blood vessel changes are closely related to cell loss (Fig. 2*F*). Most young Tg4510 mice fall within 2 SDs for both measurements, but by 15 mo, cortical thickness is reduced while blood vessel density is increased. At 18 mo, blood vessel density is less altered, with no additional change in cell loss. Thus, cell loss in this model leads to an apparent increase in blood vessel density followed by a "dying back" of blood vessel overgrowth.

**Altered Expression of Hypoxia and Angiogenesis-Related Genes in Aged Tau Mice.** Since small blood vessels in particular appear to increase in these mice and could indicate new blood vessel growth analogous to circumstances in which there is relative hypoxia or increased metabolic demand, we performed a qPCR assay to measure 84 genes related to hypoxia and angiogenesis (Fig. 3 *A*–*G*). From RNA isolates of whole cortex from 15-mo-old mice, six genes were increased more than twofold: *Lgal3*, *Lax*, *Plau*, *Hmox*, *Pgf*, and *Met* (Fig. 3*A*). The gene *Egr1* was the only gene assayed that was downregulated more than twofold.

We then sought to identify which cell type was driving these changes. We dissociated 15-mo-old mouse brains and used magnetic bead separation to isolate specific cell types (Fig. 3 *B*–*H*). RNA was then prepared from astrocytes (Fig. 3 *C* and *D*, ASCA-2–positive cells), microglia (Fig. 3 *E* and *F*, CD11b-positive cells), or endothelial cells (Fig. 3 *G* and *H*, CD31-positive cells). To validate cell enrichment of each population, cell-specific qPCR was performed and was compared with total cortical RNA from a control mouse. Astrocytes from control and Tg4510 mice were 10-fold enriched for Aquaporin-4 (*Aq4*) and were enriched slightly in *Gfap* in Tg4510 mice (Fig. 3*C*). However, astrocyte preparations also contained contaminating microglia (*Cx3xr1*) and endothelial cells (*Pecam1*). Of the 84 genes in the qPCR array, none were significantly altered in astrocytes. Microglial enrichment yielded a threefold increase in *Cx3xr1* expression and had little contamination by other cell types (Fig. 3*E*). *Lgal3*, *Serpine1*, and *Lax* were increased in Tg4510 microglia compared with controls (Fig. 3*F*). Last, the endothelial cell population was enriched 100-fold compared with whole cortex based on *Pecam1* expression, with some contaminating microglial cells (Fig. 3*G*). This population showed increased expression of *Serpine1*, *Atr*, *Plau*, *Eif4ebp*, *Slc16a3*, *VegfA*, *Hif1alpha (inhibitor)*, and *Mmp9* (Fig. 3*H*). Transcripts of neuronal RNA (*Mapt*, *Grin*, *Camk2a*) were detected in total cortical RNA but not in any of the enriched fractions. For each assay, $q$ values—the adjusted $P$ value taking into account the FDR—were calculated. CD31-positive cells, but not total RNA or CD11b cells, had significant $q$ values for all genes that also had greater than twofold changes in gene expression in the dataset. Complete statistics and gene expression data can be found in Dataset S1.

To confirm increased expression of the gene *Serpine1*, which exhibited the greatest fold change in CD31 cells, we performed Western blotting and immunofluorescence for its gene product

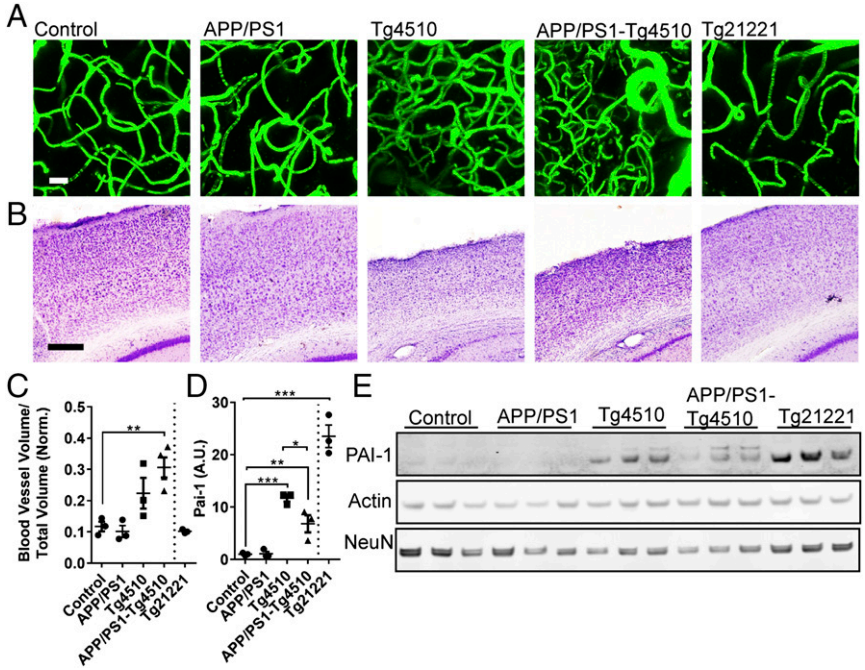


**Fig. 5.** Effects of amyloid-beta on blood vessels. (*A*) We imaged 15-mo-old mice from the APP/PS1-Tg4510 line and the related Tg21221 line (from APP/PS1-Tg21221 litters). (Scale bar, 20 μm.). $n = 3$–4 mice per genotype. (*B*) Cresyl violet-stained sections were used to measure cortical atrophy, which was observed in Tg4510 and APP/PS1-Tg4510 mice but not APP/PS1, Tg21221, or wild-type controls. (Scale bar, 200 μm.) (*C*) Blood vessel density was assessed from two-photon images and normalized to cortical thickness for each mouse. (*D* and *E*) PAI-1 was increased in mice carrying the Tg4510 (P301L tau) or Tg21221 (wild-type tau) transgene but not in APP/PS1-only mice. Beta-actin is shown as a protein loading control, and NeuN indicates neuronal protein. $^{*}P < 0.05$, $^{**}P < 0.01$, $^{***}P < 0.001$.

PAI-1 (Fig. 4). By Western blot (Fig. 4 *A* and *B*), PAI-1 was detectible in Tg4510 cortical homogenates at 2 mo and was significantly increased at 9 (Student's *t* test, $P = 0.003$, 95% CI: [2.2–6.9]) and 12 mo ($P = 0.012$, 95% CI: [6.8–33.2]) before overt blood-vessel overgrowth. PAI-1 levels remained elevated at 15 mo of age ($P = 0.03$, 95% CI: [3.9–43.8]). Immunofluorescent labeling (Fig. 4*C*) indicated that PAI-1 was increased in a heterogeneous group of cells that included neurons with neurofibrillary tangles (MC1-positive labeling) and iba-1–positive microglial cells. Additional labeling using tomato-lectin, a marker for both blood vessels and microglia (Fig. 4*D*), showed PAI-1 also overlapped with blood vessels. PAI-1 labeling was observed in Tg4510 mice and not in littermate controls at the same age.

Tg4510 mice express P301L mutant tau in neurons and develop neurofibrillary tangles and neuronal loss. We also examined a related mouse line, Tg21221, which overexpresses wild-type human tau and does not develop neurofibrillary tangles with age or neuronal loss (11, 18). In contrast to Tg4510, Tg21221 mice did not have overt vascular abnormalities (Fig. 5 *A* and *C*; Student's *t* test versus control $P = 0.39$). Cortical atrophy and loss of the neuronal marker NeuN were not observed (Fig. 5 *B* and *E*). Intriguingly though, we observed increased production of PAI-1 (Fig. 5 *D* and *E*; Student's *t* test versus control $P = 0.005$, 95% CI: [16.5–28.5]), suggesting a forme fruste of vessel-related molecular changes in Tg21221, consistent with the more severe phenotype observed in the Tg4510 line.

**Amyloid Beta Alone in APP/PS1 Mice Does not Induce Changes.** To determine if blood vessel alterations are specific to tau overexpression, we next investigated the APP/PS1 mice, which develop both diffuse and neuritic plaques by 15 mo of age, modest amyloid angiopathy, without overt neuronal loss (18–20). Compared with wild-type controls, APP/PS1 mice exhibited neither changes in blood vessel volume (Fig. 5 *A* and *C*; one-way ANOVA $P = 0.0009$, post hoc $P = 0.99$) nor cortical atrophy (Fig. 5*B*). They also did not exhibit increased PAI-1 (Fig. 5 *D* and *E*; one-way ANOVA $P < 0.0001$, control vs. APP/PS1 post hoc $P = 0.99$). Thus, in this mouse model, amyloid beta does not induce the same pathological alterations in blood vessels as observed in tau mice.

We then investigated if the presence of amyloid might enhance the tau-associated vascular phenotype at this age. APP/PS1-Tg4510 mice did have increased blood vessel volume compared with controls (Fig. 5 *A* and *C*; post hoc $P = 0.003$, 95% CI: [−0.31 to −0.07]), similar to Tg4510-only littermates ($P = 0.242$, 95% CI: [−0.20–0.038]). PAI-1 protein levels were increased in APP/PS1-Tg4510 mice compared with controls (Fig. 5 *D* and *E*; post hoc $P = 0.0008$, 95% CI: [−9.9 to −1.7]). Altogether, there was no evidence of change in the tau-induced phenotype by amyloid beta.

**Changes in Hypoxia and Angiogenesis-Related Genes in Human AD.** Since we had identified several genes including *Serpine1* (PAI-1) that were increased in tau-overexpressing mice, we evaluated 25 publicly available datasets from MSBB and Rush Medical Center (ROS/MAP), testing the hypothesis that similar changes in gene expression would occur in relationship to human tau pathology (Fig. 6*A*). Braak stages V and VI were compared with samples that were Braak 0, I, and II. The genes included in this panel were human analogs of those with twofold or greater expression change in total cortex in Tg4510 mouse (*Egr1*, *Hmox*, *Lax*, *Lgals3*, *Met*, *Plau*, and *Pgf*) as well as genes that were up-regulated in CD31-positive cells (*Atr*, *Eif4ebp*, *Hif1an*, *Mmp9*, *Serpine1*, *Slc16a3*, and *Vegfa*). In total, these datasets spanned 19 different brain regions, and all regions showed changes in at least 1 of the 14 genes assessed. Brain regions such as the nucleus accumbens, striatum, and occipital visual cortex, which are observed to have little tau pathology, showed few changes in these genes. Of the 14 genes we assessed, 7 were up-regulated with

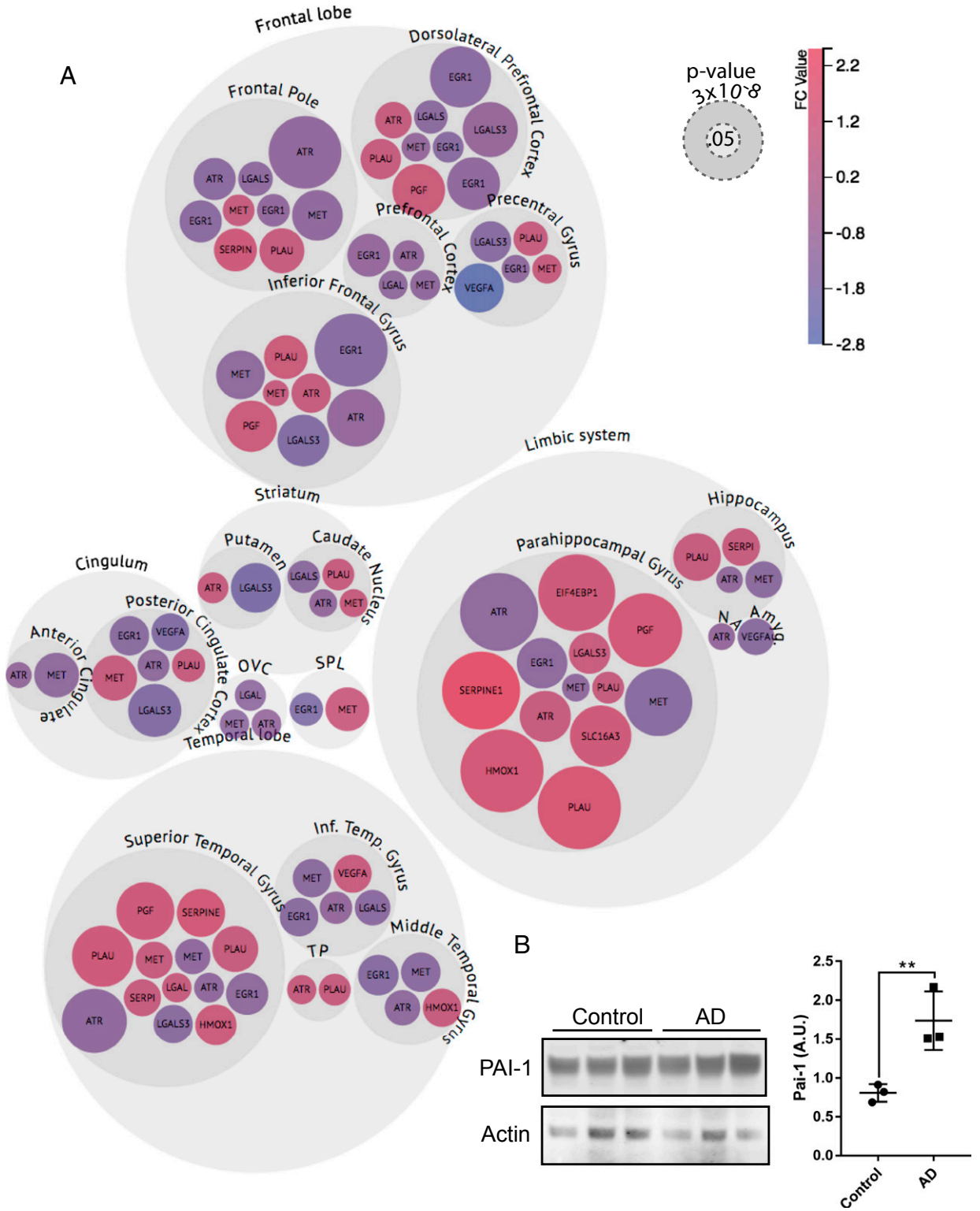


**Fig. 6.** Bubble chart analysis of gene expression changes in human brain with high neurofibrillary tangle load. (*A*) RNA expression datasets from the AMP-AD knowledge portal were assessed for differential expression of the following 14 genes, comparing Braak stages V/VI (B3) to Braak stages 0/I/II (B1): *Egr1*, *Hmox*, *Lax*, *Lgals3*, *Met*, *Plau*, *Pgf*, *Atr*, *Eif4ebp*, *Hif1an*, *Mmp9*, *Serpine1*, *Slc16a3*, and *Vegfa*. Differentially expressed genes were identified at an FDR of 25% and are listed in Dataset S2. Data are plotted by brain region. The size of each bubble is determined by the −log10(*P* value) such that highly significant changes are represented by larger bubbles. The smallest correspond to a *P* value of 0.051 and the largest 2.9 × 10E-8. The color of each bubble indicates the direction and magnitude of gene expression fold change. Genes from each dataset are shown as separate bubbles—in regions with RNA-seq and microarray data (dorsolateral prefrontal cortex, frontal pole, inferior frontal gyrus, PHG, and superior temporal gyrus), multiple bubbles per gene indicate changes in multiple datasets. NA, nucleus accumbens; OVC, occipital visual cortex; SPL, superior parietal lobe; TP, temporal pole. (*B*) Western blot of cortical homogenates from cases with low neurofibrillary tangle load (Control) versus high neurofibrillary tangle load (AD) confirmed an increase of the *Serpine1* protein product PAI-1. Beta-actin is shown for loading control. $^{**}P < 0.01$. A.U., arbitrary unit.

increasing Braak stage, particularly in classically affected regions such as the parahippocampal gyrus (PHG) and superior temporal gyrus. These genes are *Serpine1*, *Plau*, *Hmox1*, *Pgf*, *Slc16a3* (PHG only), *Eif4ebp1* (PHG only), and *Lgals3* (PHG only). The greatest increase was seen in the PHG, where *Serpine1* increased by 2.47-fold ($P < 0.0001$). *Egr1*, the only gene we observed to decrease in mice, was also reduced in multiple brain regions with increasing Braak stage including the PHG ($P = 0.02$). The remaining six genes were either not altered with FDR < 0.25 (*Hif1an*, *Lax*, *Mmp9*) or showed a fold change predominantly in the opposite direction expected (*Atr*, *Met*, *Vegfa*). For comparison in this same dataset, GFAP expression increases ranged from 1.3- to 2.3-fold in the PHG. Further, Western blotting of cortical homogenates from three Braak V/VI and three control Braak 0/I cases confirmed that PAI-1 protein was increased in AD brain (Fig. 6*B*, Student's *t* test, $P = 0.03$, 95% CI: [0.3–1.5]). Altogether, these data are consistent with alterations related to hypoxia- and/or angiogenesis-related gene programs in humans in relation to pathological tau accumulation.

## Discussion

Here we report that P301L tau expression in neurons, with accompanying neurofibrillary tangle formation and cortical atrophy, has a marked effect on cortical microvasculature, promoting increased numbers of small-diameter blood vessels that exhibit abnormal morphology and restricted red blood cell movement. These changes, including increased vessel density, are likely due to the combined effect of cortical atrophy with disease progression in addition to increased expression of angiogenesis-related genes in endothelial cells. In particular, *Serpine1* was observed to be increased in Tg4510, Tg21221, and human patient samples with tau pathology. Interestingly, Tg21221 mice did not exhibit cortical atrophy or overt blood vessel density changes but did have increased production of PAI-1, the protein product of *Serpine1*. We interpret this to mean that changes in PAI-1 expression precede overt density changes and that cortical atrophy may not be a required stimulus for this phenotype. The mechanism whereby tau induces these changes is unclear but may be related to the recent observation that tau oligomers can be detected near vessels in AD (21). Notably, accumulation of Aβ in aged APP/PS1 mice did not induce PAI-1 expression or similar blood vessel changes.

There are several implications of this work. Notably, in human AD patients, cerebral hypoperfusion is a well-established core phenotype, and the observation of diminished temporal-parietal and limbic regional cerebral blood flow is commonly used clinically in the differential diagnosis of dementia (22–25). The mechanisms underlying hypoperfusion are not known, though incidence of "string vessels" characterized by collapsed capillaries and dying endothelial cells are more prevalent (26, 27). In P301L tau-overexpressing mice, it is unclear if the very small-diameter blood vessels (<4 μm) are precursors to string vessels or are newly formed capillary tubes. However, these vessels most often lacked red blood cells and were frequently observed to contain adherent leukocytes that were restricting downstream flow to plasma only. Similarly increased spirals and turns in these vessels likely alter fluid dynamics, diminishing efficiency of nutrient delivery (28). Spiraling vessels have been noted in human AD (29, 30). Together, changes observed in vivo in tau-overexpressing mice support hypoperfusion observations in AD.

We also show that changes in vessel density are dynamic. Density appeared to increase between 12 and 15 mo and appeared to decline thereafter. Studies of capillary density in human AD are conflicting (30–34). While discrepancies may be explained by variation in regions analyzed, it may also be that capillary density is only transiently increased in human patients as well and is dependent on disease stage. Addition of Aβ in APP/PS1-Tg4510 mice did not appear to enhance this phenotype, though a previous report indicates that 18–24-mo-old Tg2576 mice expressing the $APP_{SWE}$ mutation exhibit increased CD105, which is primarily expressed in endothelial cells (35). Thus, further studies are required to assess the combined effect of both Aβ and tau pathology in this context. How other pathological lesions, including the comorbidities that contribute to small-vessel disease in humans like diabetes or hypertension, act synergistically to alter the course of vessel changes will be important for understanding the human disease course.

PAI-1 is a serine protease inhibitor and a classic regulator of the plasminogen activation pathway. It has been well-characterized in tumor angiogenesis, where high levels are associated with poor outcomes in certain cancer types (36, 37). In the brain, PAI-1 is expressed by neurons, astrocytes, and microglia in addition to endothelial cells (38–40). Notably, in microglial cells, PAI-1 regulates motility and phagocytosis, and increased PAI-1 colocalization in microglia from Tg4510 mice was observed, in agreement with qPCR results (40). We also observed colocalization of PAI-1 with neurofibrillary tangles, which has been previously reported, though the relevance of this to disease is unknown (41). In endothelial cells, PAI-1 stimulates migration and regulates proteolytic activity, which is important for extracellular remodeling during angiogenesis (38, 42). Other key components of this system include VEGFA, uPA (urokinase-type plasminogen activator; *Plau*), and MMP9 (matrix metalloproteinase 9), which were all upregulated in endothelial cells isolated from Tg4510 mice (43, 44). Altogether, increased expression of multiple proteins involved in vascular remodeling pathways provides strong evidence for the induction of angiogenesis in this model.

Further implicating this pathway in neurodegenerative disease, increased VEGFA and PAI-1 have both been reported in brain, cerebrospinal fluid, and serum from AD patients; while they are not specific for the disease, when used in biomarker panels, they may improve diagnostics (45–52). VEGFA, importantly, is a known inducer of microvascular permeability that could mechanistically explain the previously observed increases in blood–brain barrier permeability in the Tg4510 mouse model (23, 53).

These data indicate that tau overexpression in neurons can lead to dramatic, cell-nonautonomous changes in cerebral endothelial cells. While recent data have highlighted glial–neuronal interactions in neurodegenerative disease, these are the first data to directly implicate neuronal tau pathology in endothelial biology and Alzheimer's-related vascular remodeling (54). It remains unclear how specific cellular signals lead to these changes and whether a direct interaction between tau and endothelial cells exists. However, the analysis of both mouse and human samples suggest that tau-induced neurodegeneration contributes to vascular abnormalities and may help explain the underlying cause of these changes in patients. An analogous situation occurs in macular degeneration, where dramatic neovascular changes accompany neurodegeneration. In the case of macular degeneration, anti-VEGF treatments not only impact the vascular changes but dramatically halt progressive deterioration in many patients (55). This raises the possibility that targeting these tau-induced vascular changes may be beneficial in slowing the progression of AD.

**ACKNOWLEDGMENTS.** We thank P. Davies for providing the MC1 anti-tau antibody used in this study and the patients and their families for their selfless donation to further understanding AD. We acknowledge the donors of Alzheimer's Disease Research, a program of BrightFocus Foundation, for support of this research. This research was funded by NIA training grants to the Division of Medical Sciences at Harvard University (NIH/NIA Grant T32 AG000222, to R.E.B.) and by NIH Grants AG026249 and AG005134. Human gene expression data were obtained from the AMP-AD Knowledge Portal and were generated from postmortem brain tissue collected through the Mount Sinai VA Medical Center Brain Bank and provided by Dr. Eric Schadt from Mount Sinai School of Medicine. Additional study data were provided by the Rush Alzheimer's Disease Center, Rush University Medical Center, Chicago. Data collection was supported through funding by NIA Grants P30AG10161, R01AG15819, R01AG17917, R01AG30146, R01AG36836, U01AG32984, and U01AG46152; the Illinois Department of Public Health; and the Translational Genomics Research Institute.

1. Chui HC, Ramirez-Gomez L (2015) Clinical and imaging features of mixed Alzheimer and vascular pathologies. *Alzheimers Res Ther* 7:21.
2. Attems J, Jellinger KA (2014) The overlap between vascular disease and Alzheimer's disease—Lessons from pathology. *BMC Med* 12:206.
3. Hofman A, et al. (1997) Atherosclerosis, apolipoprotein E, and prevalence of dementia and Alzheimer's disease in the Rotterdam Study. *Lancet* 349:151–154.
4. Launer LJ, et al. (2010) Lowering midlife levels of systolic blood pressure as a public health strategy to reduce late-life dementia: Perspective from the Honolulu Heart Program/Honolulu Asia Aging Study. *Hypertens* 55:1352–1359.
5. Ott A, et al. (1999) Diabetes mellitus and the risk of dementia: The Rotterdam Study. *Neurology* 53:1937–1942.
6. Pappolla MA, et al. (2003) Mild hypercholesterolemia is an early risk factor for the development of Alzheimer amyloid pathology. *Neurology* 61:199–205.
7. Bradley KM, et al. (2002) Cerebral perfusion SPET correlated with Braak pathological stage in Alzheimer's disease. *Brain* 125:1772–1781.
8. Smith R, et al. (2017) Tau neuropathology correlates with FDG-PET, but not AV-1451-PET, in progressive supranuclear palsy. *Acta Neuropathol* 133:149–151.
9. Boulouis G, et al. (2017) Small vessel disease burden in cerebral amyloid angiopathy without symptomatic hemorrhage. *Neurology* 88:878–884.
10. Santacruz K, et al. (2005) Tau suppression in a neurodegenerative mouse model improves memory function. *Science* 309:476–481.
11. Hoover BR, et al. (2010) Tau mislocalization to dendritic spines mediates synaptic dysfunction independently of neurodegeneration. *Neuron* 68:1067–1081.
12. Bennett RE, et al. (2017) Enhanced tau aggregation in the presence of amyloid β. *Am J Pathol* 187:1601–1612.
13. Reichenbach ZW, Li H, Gaughan JP, Elliott M, Tuma R (2015) IV and IP administration of rhodamine in visualization of WBC-BBB interactions in cerebral vessels. *Microsc Res Tech* 78:894–899.
14. Braak H, Braak E (1991) Neuropathological stageing of Alzheimer-related changes. *Acta Neuropathol* 82:239–259.
15. Ritchie ME, et al. (2015) Limma powers differential expression analyses for RNA-sequencing and microarray studies. *Nucleic Acids Res* 43:e47.
16. Benjamini Y, Hochberg Y (1995) Controlling the false discovery rate: A practical and powerful approach to multiple testing. *J R Stat Soc B* 57:289–300.
17. Stefanovic B, et al. (2008) Functional reactivity of cerebral capillaries. *J Cereb Blood Flow Metab* 28:961–972.
18. Jackson RJ, et al. (2016) Human tau increases amyloid β plaque size but not amyloid β-mediated synapse loss in a novel mouse model of Alzheimer's disease. *Eur J Neurosci* 44:3056–3066.
19. Jankowsky JL, et al. (2004) Mutant presenilins specifically elevate the levels of the 42 residue beta-amyloid peptide in vivo: Evidence for augmentation of a 42-specific gamma secretase. *Hum Mol Genet* 13:159–170.
20. Garcia-Alloza M, et al. (2006) Characterization of amyloid deposition in the APPswe/PS1dE9 mouse model of Alzheimer disease. *Neurobiol Dis* 24:516–524.
21. Castillo-Carranza DL, et al. (2017) Cerebral microvascular accumulation of tau oligomers in Alzheimer's disease and related tauopathies. *Aging Dis* 8:257–266.
22. Thomas T, Miners S, Love S (2015) Post-mortem assessment of hypoperfusion of cerebral cortex in Alzheimer's disease and vascular dementia. *Brain* 138:1059–1069.
23. Dvorak HF, Nagy JA, Feng D, Brown LF, Dvorak AM (1999) Vascular permeability factor/vascular endothelial growth factor and the significance of microvascular hyperpermeability in angiogenesis. *Curr Top Microbiol Immunol* 237:97–132.
24. Roher AE, et al. (2011) Transcranial doppler ultrasound blood flow velocity and pulsatility index as systemic indicators for Alzheimer's disease. *Alzheimers Dement* 7:445–455.
25. Alsop DC, Dai W, Grossman M, Detre JA (2010) Arterial spin labeling blood flow MRI: Its role in the early characterization of Alzheimer's disease. *J Alzheimers Dis* 20:871–880.
26. Hunter JM, et al. (2012) Morphological and pathological evolution of the brain microcirculation in aging and Alzheimer's disease. *PLoS One* 7:e36893.
27. Brown WR (2010) A review of string vessels or collapsed, empty basement membrane tubes. *J Alzheimers Dis* 21:725–739.
28. de la Torre JC (1994) Impaired brain microcirculation may trigger Alzheimer's disease. *Neurosci Biobehav Rev* 18:397–401.
29. Hassler O (1967) Arterial deformities in senile brains. The occurrence of the deformities in a large autopsy series and some aspects of their functional significance. *Acta Neuropathol* 8:219–229.
30. Fischer VW, Siddiqi A, Yusufaly Y (1990) Altered angioarchitecture in selected areas of brains with Alzheimer's disease. *Acta Neuropathol* 79:672–679.
31. Bell MA, Ball MJ (1981) Morphometric comparison of hippocampal microvasculature in ageing and demented people: Diameters and densities. *Acta Neuropathol* 53:299–318.
32. Desai BS, Schneider JA, Li J-L, Carvey PM, Hendey B (2009) Evidence of angiogenic vessels in Alzheimer's disease. *J Neural Transm (Vienna)* 116:587–597.
33. Götz J, Chen F, van Dorpe J, Nitsch RM (2001) Formation of neurofibrillary tangles in P301l tau transgenic mice induced by Abeta 42 fibrils. *Science* 293:1491–1495.
34. Buée L, et al. (1994) Pathological alterations of the cerebral microvasculature in Alzheimer's disease and related dementing disorders. *Acta Neuropathol* 87:469–480.
35. Biron KE, Dickstein DL, Gopaul R, Jefferies WA (2011) Amyloid triggers extensive cerebral angiogenesis causing blood brain barrier permeability and hypervascularity in Alzheimer's disease. *PLoS One* 6:e23789.
36. Bajou K, et al. (2001) The plasminogen activator inhibitor PAI-1 controls in vivo tumor vascularization by interaction with proteases, not vitronectin. Implications for anti-angiogenic strategies. *J Cell Biol* 152:777–784.
37. Pedersen H, et al. (1994) Prognostic impact of urokinase, urokinase receptor, and type 1 plasminogen activator inhibitor in squamous and large cell lung cancer tissue. *Cancer Res* 54:4671–4675.
38. Isogai C, et al. (2001) Plasminogen activator inhibitor-1 promotes angiogenesis by stimulating endothelial cell migration toward fibronectin. *Cancer Res* 61:5587–5594.
39. Hultman K, et al. (2010) Expression of plasminogen activator inhibitor-1 and protease nexin-1 in human astrocytes: Response to injury-related factors. *J Neurosci Res* 88:2441–2449.
40. Jeon H, et al. (2012) Plasminogen activator inhibitor type 1 regulates microglial motility and phagocytic activity. *J Neuroinflammation* 9:149.
41. Hino H, et al. (2001) Immunohistochemical localization of plasminogen activator inhibitor-1 in rat and human brain tissues. *Neurosci Lett* 297:105–108.
42. Czekay R-P, et al. (2011) PAI-1: An integrator of cell signaling and migration. *Int J Cell Biol* 2011:562481.
43. Rempe RG, Hartz AM, Bauer B (2016) Matrix metalloproteinases in the brain and blood-brain barrier: Versatile breakers and makers. *J Cereb Blood Flow Metab* 36:1481–1507.
44. Breuss JM, Uhrin P (2012) VEGF-initiated angiogenesis and the uPA/uPAR system. *Cell Adhes Migr* 6:535–615.
45. Craig-Schapiro R, et al. (2011) Multiplexed immunoassay panel identifies novel CSF biomarkers for Alzheimer's disease diagnosis and prognosis. *PLoS One* 6:e18850.
46. Oh J, Lee H-J, Song J-H, Park SI, Kim H (2014) Plasminogen activator inhibitor-1 as an early potential diagnostic marker for Alzheimer's disease. *Exp Gerontol* 60:87–91.
47. Sutton R, Keohane ME, VanderBerg SR, Gonias SL (1994) Plasminogen activator inhibitor-1 in the cerebrospinal fluid as an index of neurological disease. *Blood Coagul Fibrinolysis* 5:167–171.
48. Akenami FO, Koskiniemi M, Färkkilä M, Vaheri A (1997) Cerebrospinal fluid plasminogen activator inhibitor-1 in patients with neurological disease. *J Clin Pathol* 50:157–160.
49. Chiappelli M, et al. (2006) VEGF gene and phenotype relation with Alzheimer's disease and mild cognitive impairment. *Rejuvenation Res* 9:485–493.
50. Tarkowski E, et al. (2002) Increased intrathecal levels of the angiogenic factors VEGF and TGF-beta in Alzheimer's disease and vascular dementia. *Neurobiol Aging* 23:237–243.
51. Gerenu G, et al. (2017) Modulation of BDNF cleavage by plasminogen-activator inhibitor-1 contributes to Alzheimer's neuropathology and cognitive deficits. *Biochim Biophys Acta* 1863:991–1001.
52. Magistri M, Velmeshev D, Makhmutova M, Faghihi MA (2015) Transcriptomics profiling of Alzheimer's disease reveal neurovascular defects, altered amyloid-β homeostasis, and deregulated expression of long noncoding RNAs. *J Alzheimers Dis* 48:647–665.
53. Bates DO, Curry FE (1996) Vascular endothelial growth factor increases hydraulic conductivity of isolated perfused microvessels. *Am J Physiol* 271:H2520–H2528.
54. Chung W-S, Welsh CA, Barres BA, Stevens B (2015) Do glia drive synaptic and cognitive impairment in disease? *Nat Neurosci* 18:1539–1545.
55. Rosenfeld PJ, et al.; MARINA Study Group (2006) Ranibizumab for neovascular age-related macular degeneration. *N Engl J Med* 355:1419–1431.